IAEA
International Atomic Energy Agency

INDC(CCP)-0449
Distr. Web only

INDC International Nuclear Data Committee

Measuring the neutron field characteristics of the outside surface of the 0.8 GeV proton-irradiated «thick» W-Na target

Prepared by

Yu. E. Titarenko
Institute for Theoretical and Experimental Physics (ITEP)

Co-authors: V.F. Batyaev, E.I. Karpikhin, V.M. Zhivun,
Institute for Theoretical and Experimental Physics (ITEP)

October 2009

Selected INDC documents may be downloaded in electronic form from
http://www-nds.iaea.org/indc_sel.html or sent as an e-mail attachment.
Requests for hardcopy or e-mail transmittal should be directed to *services@iaeand.iaea.org*
or to:
Nuclear Data Section
International Atomic Energy Agency
Vienna International Centre
PO Box 100
A-1400 Vienna
Austria

Printed by the IAEA in Austria

October 2009

INDC(CCP)-0449
Distr. Web only

Measuring the neutron field characteristics of the outside surface of the 0.8 GeV proton-irradiated «thick» W-Na target

Prepared by

Yu.E. Titarenko
Institute for Theoretical and Experimental Physics (ITEP)

Co-authors: V.F. Batyaev, E.I. Karpikhin, V.M. Zhivun,
Institute for Theoretical and Experimental Physics (ITEP)

Abstract

The main goal of the Project is to study and evaluate nuclear characteristics of materials and isotopes involved in processes of irradiated nuclear fuel transmutation. This principal task is subdivided into 9 subtasks subject to the neutron or proton source used, the type of the nuclear process under study, isotope collection, characteristics of which are to be investigated, etc. In the presented extract of the Project Activity report the measurements there were used the threshold activation reaction rates in ^{12}C, ^{19}F, ^{27}Al, ^{59}Co, ^{63}Cu, ^{65}Cu, ^{64}Zn, ^{93}Nb, ^{115}In, ^{169}Tm, ^{181}Ta, ^{197}Au, and ^{209}Bi thin samples placed inside and outside the 0.8-GeV proton-irradiated 4-cm thick W target and 92-cm thick W-Na composite target of 15-cm diameter both. In total, more than 1000 values of activation reaction were determined in the both experiments. The measured reaction rates were compared with the rates simulated by the LAHET code with the use of several nuclear databases for the respective excitation functions, namely, MENDL2 together with MENDL2P for cross sections of protons and neutrons up to 100 MeV, and recently developed IEAF-2001 that provides neutron cross sections up to 150 MeV. The comparison between the simulation-to-experiment agreements obtained via the MENDL2 and IEAF-2001 is presented. The agreement between simulation and experiment has been found general satisfactory for both of the databases. However, further studies should be conducted for the purposes of perfecting the simulation of the production of secondary protons and high-energy neutrons, as well as the high-energy neutron elastic scattering. The results obtained permit some conclusions concerning the reliability of the transport codes and data bases used to simulate the Accelerator Driven Systems (ADS), particularly with Na-cooled W targets. The high-energy threshold excitation functions to be used in the activation-based unfolding of neutron spectra inside the ADS can also be inferred from the results.

October 2009

Contents

G - MEASURING THE NEUTRON FIELD CHARACTERISTICS OF THE OUTSIDE SURFACE OF THE 0.8 GEV PROTON-IRRADIATED «THICK» W-NA TARGET

1 Experimental design

The 0.8 GeV proton beam from the ITEP U-10 accelerator was used to study the neutron field characteristics.

1.1 The W-Na target

The target is assembled of the alternating W and Na discs. Fig. 1 is the target assembly view. The W discs total to 12 and are 150-mm diameter all-metal pellets of 40-mm (seven pieces) and 20-mm (five pieces) depths. The discs have been manufactured of the WNF-97.5 alloy (a mixture of 97.50% W, 1.75% Ni, and 0.75% Fe powders) by the powder metallurgy techniques (hydrostatic compaction + sintering in hydrogen + vacuum annealing). Table 1 presents the composition of the input materials. The job-oriented "rulers" inserted into the discs are intended for placing the sampled to be irradiated.

The Na discs total to 13 and are the stainless sheet steel cylinder-shaped containers (tanks) of 150-mm diameter, 40-mm height filled with metallic Na. Table 2 presents the Na composition.

Table 3 presents the sequence and the main parameters of the discs. The disc arrangement was so selected that the longitudinal distribution of the secondary neutron flux over the target side surface would be as uniform as possible.

To be irradiated, the target was placed on the positioning table of special design.

The positioning table houses the W-Na target and fixes the latter in the vertical and horizontal planes. The table consists of the base, load-bearing plate, and support-cradle assembly and has been designed to be demountable, so that the cradle with the W-Na target irradiated could be transported immediately after irradiation to the protective container.

The base (drawing PT.010.AS) consists of the lower and upper plates (PT.021 and PT.024, respectively).The upper and lower plates are welded together through six ribs (PT.022) and four ribs (PT.023). Six boards (PT.025) are welded from below to the lower plate (PT.021). The upper plate has four holes to receive the axle studs (PT.017).

The load-bearing plate (PT.020.AS) consists of the lower and upper plates (PT.031 and Pt.034, respectively). The two plates are welded together through two ribs (PT.032) and four ribs (PT.033).

The load bearing plate can be shifted vertically by screwing up the nuts (PT.001) on the axle studs (PT.017).

The front and back devices for horizontal shifting the support (PT.030.AS) with the cradle that carries the W-Na target consist of the lead screws (PT.002) and clevis rods (PT.004). The lead screws are fastened with the bushings (PT.003) on either sides in the load-bearing plate (PT.020.AS). The bashing are fastened with bolts M6-6gx14.23 (Ref. No. 29; 24 pieces) to the load-bearing plate. When positioning the target, the lead screws are turned with the handle (PT.070.AS).

The support (PT.030.AS) consists of the plate (PT.041), two ribs (PT.043), the wall (PT.042), and the rest (PT.046). All the parts are welded together. The ribs (PT.045; 8 pieces) and the rests (PT.044 and PT.046) are inserted for stiffness. The back hinged flap (PT.040) is fastened with the arms (PT.047 and PT.049) and clamp (PT.048) welded to the wall (PT.042).

The hinged flap (PT.040) fixes the W-Na target in the cradle and consists of the plate (PT.061), the lug (PT.062), the post (PT.063), and the eye bolt (PT.064). All the parts are fastened by welding. The

hinged flap (PT.040) is fastened to the support (PT.030.AS) by the axle (PT.008). The lock is assembled of the axle (PT.007), the bushing (PT.006), and the lever (PT.016). The target is squeezed with three screws (PT.013).

The cradle (PT.060.AS) consists of the bed (PT.081), to which the front and back rests (PT.082 and PT.083) are welded to fix the target. The cradle is precisely positioned on the support (PT.030.AS) by four lugs (PT.084) welded to the cradle. The remote-controlled transportation cable is fastened to the bottom of the bed (PT.081) with the following fasteners: studs M4-6gx24.07.AD1 (Ref. No. 38; 4 pieces), washers (Ref. No. 33) nuts (Ref. No. 32), planks (PT.015), bolts M5-6gx50.AD1 (Ref. No. 28), washers (Ref. No. 34), and catches (PT.014).

1.2 Experimental samples

In the experiments, the absolute reaction rates are determined for ^{209}Bi, ^{197}Au, ^{169}Tm, ^{115}In, ^{93}Nb, ^{65}Cu, ^{64}Zn, ^{63}Cu, ^{59}Co, ^{27}Al, ^{19}F, and ^{12}C. Table 4 presents the parameters of the samples. The results of certifying the samples can be found in Table 5. The layout of the samples in the target is shown in Figs. 1-4 and Table 4. The samples are placed on either the W disc lateral faces or the seats (slots) in the W-made rulers. The locations of the samples are marked A, B, C, D, E on the rulers, and S, L, R, M, I, J, K on the disc outsides. The markers are strictly coaxial in all the discs, i.e., identical markers on different discs are lined up along the target axis. The arrangement of the samples is identical on the first, third, fifth, and seventh discs (see Fig. 2). Fig. 3 shows the arrangement of the samples on the second disc. The arrangements of the samples on the fourth, sixth, eighth, ninth, and tenth discs are shown in Fig. 4.

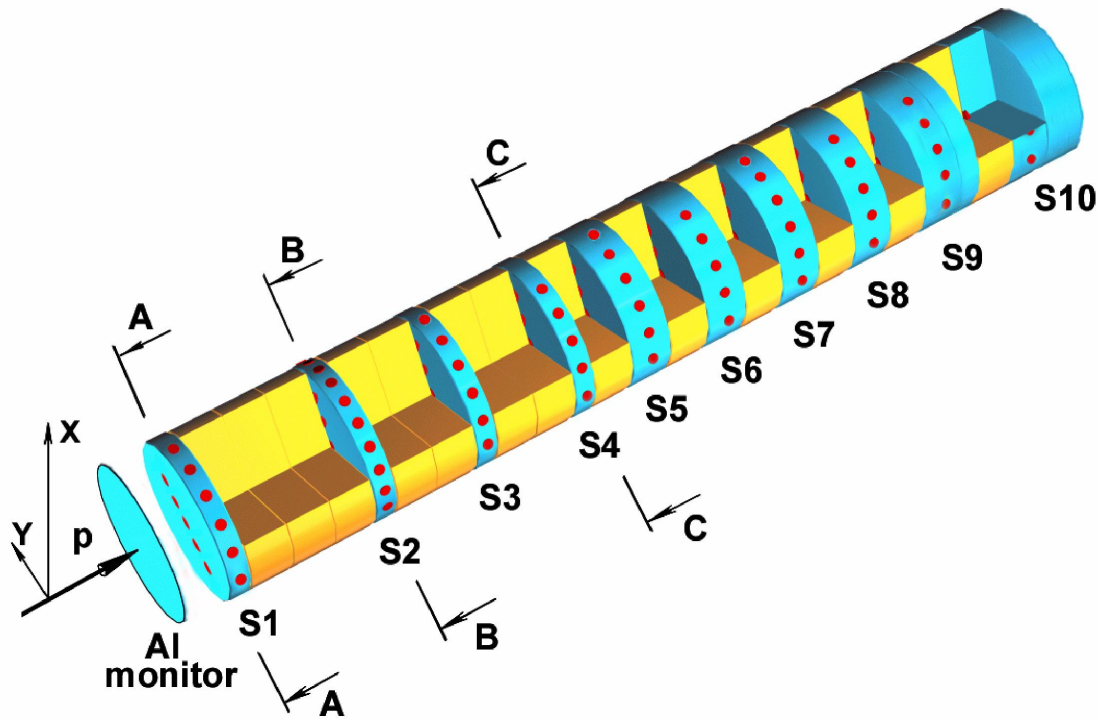

Fig. 1. The W-Na target assembly view.

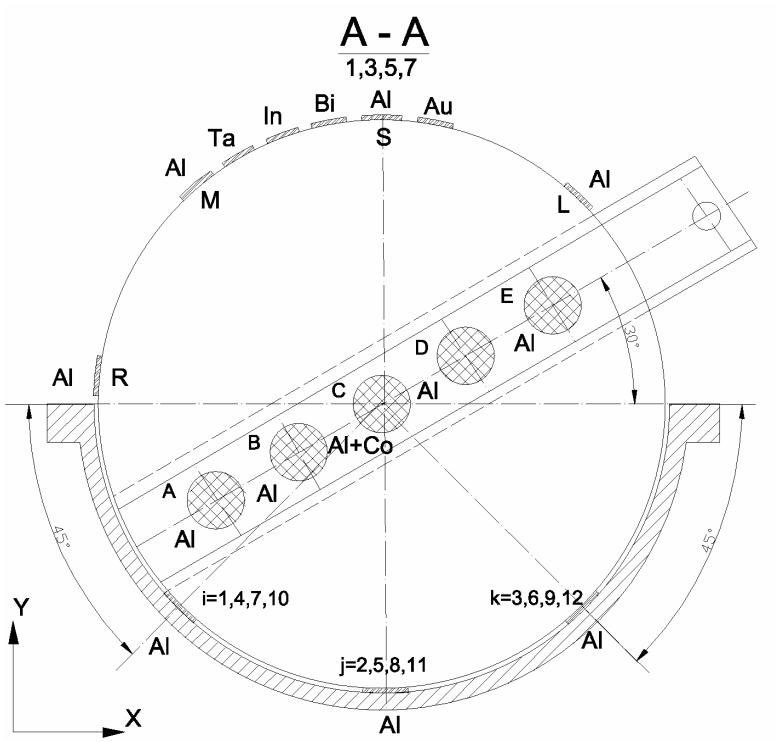

Fig. 2. The A-A section of the target assembly view. Layout of the samples on the first, third, fifth, and seventh discs.

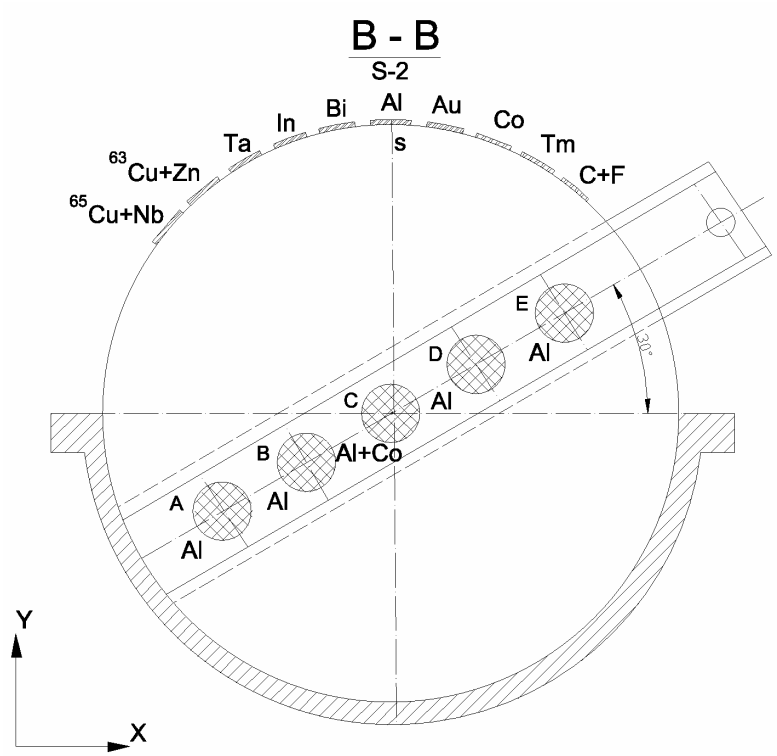

Fig. 3. The B-B section of the target assembly view. Layout of the samples on the second disc.

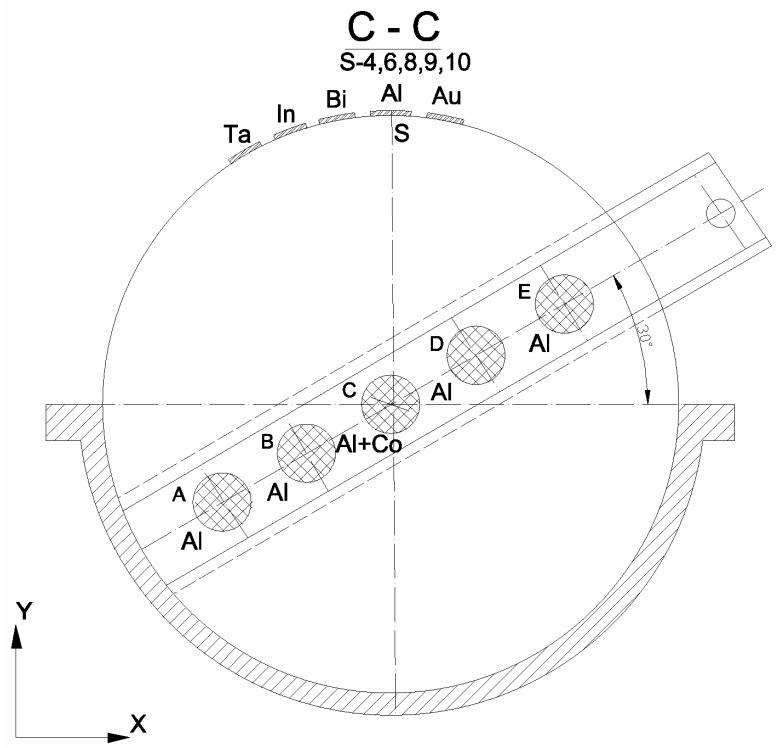

Fig. 4. The C-C section of the target assembly view. Layout of the samples on the fourth, sixth, eighth, ninth, and tenth discs.

Table 1. Composition of the input materials to manufacture the W discs.

W (PVZK grade)		Ni (PNK1L5 grade)		Fe (PZhR3.200.28 grade)	
Element	% mass	Element	% mass	Element	% mass
Fe	$7 \cdot 10^{-3}$	Co	$<1 \cdot 10^{-3}$	C	$1 \cdot 10^{-3}$
Ni	$3 \cdot 10^{-3}$	Cu	$<1 \cdot 10^{-3}$	Si	$4 \cdot 10^{-3}$
Si	$3 \cdot 10^{-3}$	Fe	$1 \cdot 10^{-3}$	Mg	$8 \cdot 10^{-3}$
Ca	$2 \cdot 10^{-3}$	Si	$1 \cdot 10^{-3}$	S	$1.3 \cdot 10^{-3}$
P	$2 \cdot 10^{-3}$	S	$1 \cdot 10^{-3}$	P	$1.4 \cdot 10^{-3}$
S	$1 \cdot 10^{-3}$	C	$1.2 \cdot 10^{-1}$	O	$2.2 \cdot 10^{-2}$
Humidity + O_2	$1 \cdot 10^{-1}$	Pb	$<1 \cdot 10^{-4}$	Humidity	$3 \cdot 10^{-4}$
Mo	$2 \cdot 10^{-2}$	As	$<1 \cdot 10^{-4}$	Fe	99.962
Al	$2 \cdot 10^{-2}$	Sb	$<2 \cdot 10^{-4}$		
W	99.95	Sn	$<1 \cdot 10^{-4}$		
		Bi	$<1 \cdot 10^{-4}$		
		P	$<1 \cdot 10^{-3}$		
		Zn	$<1 \cdot 10^{-3}$		
		Cd	$<1 \cdot 10^{-4}$		
		Mg	$<1 \cdot 10^{-3}$		
		Mn	$<310^{-4}$		
		Ni	99.87		

Table 2. The results of spectral analysis of sampled Na metal (mass%).

Element	% mass	Element	% mass
Fe	$<1 \cdot 10^{-3}$	Pb	$<1 \cdot 10^{-3}$
Mg	$<1 \cdot 10^{-4}$	Ti	$<3 \cdot 10^{-3}$
Al	$<1 \cdot 10^{-3}$	Bi	$<1 \cdot 10^{-3}$
Cu	$<1 \cdot 10^{-4}$	Ni	$<1 \cdot 10^{-3}$
Ba	$<3 \cdot 10^{-3}$	Ag	$<1 \cdot 10^{-4}$
Cd	$<1 \cdot 10^{-4}$	V	$<1 \cdot 10^{-3}$
Be	$<3 \cdot 10^{-5}$	Co	$<1 \cdot 10^{-3}$
Mn	$<1 \cdot 10^{-4}$	Mo	$<3 \cdot 10^{-3}$
Sn	$<2 \cdot 10^{-3}$	Zn	$<1 \cdot 10^{-2}$
Cr	$<1 \cdot 10^{-3}$	Ca	$8 \cdot 10^{-4}$

1.3 Irradiation

The target to be 0.8 GeV proton-irradiated was placed on the positioning table. The irradiation time was T = 35 952 s. During the irradiation. the proton pulse intensity was monitored by measuring the pulse amplitude in the output of the integral ionization chamber. The results are shown in Fig. 5.

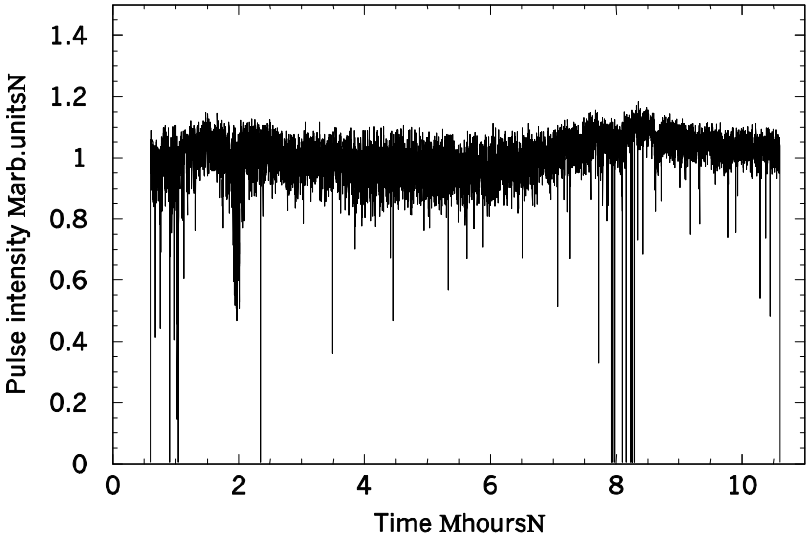

Fig. 5. The proton beam intensity variations during the irradiation run.

Table 3. Parameters of W and Na discs.

Nos.	Disc, ruler	Thickness, mm	Mass, g	Mean density, g/cm^3
1	W-Disk W-Ruler	20	6270.5 336.2	18.59 18.55
2	Na-Disk	40	620.12	0.915
3	Na-Disk	40	638.735	0.942
4	Na-Disk	40	620.36	0.915
5	W-Disk W-Ruler	20	6240.4 336.6	18.6 18.65
6	Na-Disk	40	643.49	0.949
7	Na-Disk	40	622.28	0.918
8	W-Disk W-Ruler	20	6220.7 334.2	18.58 18.55
9	Na-Disk	40	624.63	0.921
10	Na-Disk	40	628.61	0.927
11	W-Disk W-Ruler	20	6219.8 332.5	18.53 18.68
12	Na-Disk	40	621.91	0.917
13	W-Disk W-Ruler	40	12777 333.5	18.57 18.54
14	Na-Disk	40	615.86	0.908
15	W-Disk W-Ruler	40	12813.1 333.1	18.6 18.63
16	Na-Disk	40	634.02	0.935
17	W-Disk W-Ruler	40	12850.5 335.1	18.65 18.59
18	Na-Disk	40	626.68	0.924
19	W-Disk W-Ruler	40	12769.5 332	18.55 18.6
20	Na-Disk	40	625.61	0.923
21	W-Disk W-Ruler	40	12778.2 330.4	18.55 18.49
22	W-Disk W-Ruler	20	6230 336.5	18.57 18.68
23	Na-Disk	47	713.22	0.893
24	W-Disk W-Ruler	40	12808.3 322.7	18.59 18.61
25	W-Disk W-Ruler	40	12815.1 329.2	18.61 18.63

Table 4. Parameters of experimental samples.

W disc Nos.	Samples inside the target			Samples on the target outside		
	Sample	Diameter, mm	Weight, mg	Material	Diameter, mm	Weight, mg
1	Al(A)	10.5	151.3	Bi	10.5	1809.0
	Al(B)	10.5	133.6	Au	10.0	156.4
	Al(C)	10.5	30.0	^{115}In	10.5	503.7
	Co(C)	10.5	203.8	Al(S)	10.5	331.5
	Al(D)	10.5	130.8	Ta	10.0	267.9
	Al(E)	10.5	131.7	Al(L)	10.5	331.2
				Al(M)	10.5	332.7
				Al(R)	10.5	337.7
				Al(I)	10.5	119.4
				Al(J)	10.5	119.2
				Al(K)	10.5	118.3
2	Al(A)	10.5	117.7	Bi	10.5	1785.7
	Al(B)	10.5	117.9	Au	10.0	154.9
	Al(C)	10.5	29.8	^{115}In	10.5	487.2
	Co(C)	10.5	205.7	Al(S)	10.5	327.5
	Al(D)	10.5	121.8	C	10.5	286.4
	Al(E)	10.5	126.5	F_2C	10.5	369.5
				Co	10.5	1765.0
				^{64}Zn	10.5	855.3
				^{63}Cu	10.5	3647.0
				^{65}Cu	10.5	761.0
				Nb	10.0	211.5
				Tm	10.5	493.0
				Ta	10.0	267.1
3	Al(A)	10.5	136.1	Bi	10.5	1773.3
	Al(B)	10.5	136.9	Au	10.0	153.8
	Al(C)	10.5	30.3	^{115}In	10.5	505.0
	Co(C)	10.5	207.1	Al(S)	10.5	330.2
	Al(D)	10.5	137.9	Ta	10.0	267.2
	Al(E)	10.5	139.7	Al(L)	10.5	335.8
				Al(M)	10.5	340.8
				Al(R)	10.5	337.1
				Al(I)	10.5	118.8
				Al(J)	10.5	118.5
				Al(K)	10.5	119.4
4	Al(A)	10.5	140.2	Bi	10.5	1824.7
	Al(B)	10.5	140.3	Au	10.0	155.2
	Al(C)	10.5	59.5	^{115}In	10.5	611.8
	Co(C)	10.5	207.0	Al(S)	10.5	330.8
	Al(D)	10.5	146.2	Ta	10.0	
	Al(E)	10.5	146.3			

Table 4. contn'd.

W disc Nos.	Samples inside the target			Samples on the target outside		
	Sample	Diameter, mm	Weight, mg	Material	Diameter, mm	Weight, mg
5	Al(A)	10.5	128.5	Bi	10.5	1796.0
	Al(B)	10.5	151.2	Au	10.0	156.1
	Al(C)	10.5	59.5	^{115}In	10.5	518.5
	Co(C)	10.5	207.0	Al(S)	10.5	327.5
	Al(D)	10.5	147.4	Ta	10.0	267.8
	Al(E)	10.5	135.3	Al(L)	10.5	335.1
				Al(M)	10.5	336.4
				Al(R)	10.5	316.4
				Al(I)	10.5	120.3
				Al(J)	10.5	119.2
				Al(K)	10.5	118.5
6	Al(A)	10.5	133.9	Bi	10.5	1774.6
	Al(B)	10.5	144.0	Au	10.0	156.3
	Al(C)	10.5	59.3	^{115}In	10.5	497.8
	Co(C)	10.5	203.3	Al(S)	10.5	330.8
	Al(D)	10.5	139.4	Ta	10.0	268.3
	Al(E)	10.5	133.3			
7	Al(A)	10.5	147.7	Bi	10.5	1797.8
	Al(B)	10.5	131.8	Au	10.0	155.7
	Al(C)	10.5	60.0	^{115}In	10.5	502.3
	Co(C)	10.5	206.7	Al(S)	10.5	329.9
	Al(D)	10.5	141.0	Ta	10.0	268.3
	Al(E)	10.5	124.3	Al(L)	10.5	318.5
				Al(M)	10.5	339.3
				Al(R)	10.5	332.0
				Al(I)	10.5	119.0
				Al(J)	10.5	119.0
				Al(K)	10.5	118.4
8	Al(A)	10.5	139.8	Bi	10.5	1830.9
	Al(B)	10.5	143.4	Au	10.0	157.9
	Al(C)	10.5	110.3	^{115}In	10.5	496.6
	Co(C)	10.5	206.9	Al(S)	10.5	327.8
	Al(D)	10.5	153.9	Ta	10.0	267.1
	Al(E)	10.5	139.5			
9	Al(C)	10.5	110.2	Bi	10.5	1758.8
	Co(C)	10.5	205.0	Au	10.0	155.9
	Al(A)	10.5	141.1	^{115}In	10.5	485.0
	Al(B)	10.5	143.7	Al(S)	10.5	328.4
	Al(D)	10.5	142.0	Ta	10.0	267.3
	Al(E)	10.5	142.1			
10	Al(A)	10.5	144.2	Bi	10.5	1793.9
	Al(B)	10.5	148.6	Au	10.0	156.7
	Al(C)	10.5	220.8	^{115}In	10.5	517.8
	Co(C)	10.5	410.0	Al(S)	10.5	329.5
	Al(D)	10.5	152.5	Ta	10.0	268.5
	Al(E)	10.5	150.4			

Total: 142 samples

Table 5. Certification of experimental samples.

Nos.	Sample (placing marked)	Composition (components of content above 0.1% are presented)	Certificate
1	^{12}C	Extremely-high pure	
2	$^{19}F_2C$(Teflon)	Extremely-high pure	
3	^{27}Al(C1-C3)	Al-99.99%	ALDRICH – Nr 32,686-0
4	^{27}Al(C4-C7)	Al-99.999%	ALDRICH - Nr 32,685-2
5	^{27}Al(C8-C10)	Al-99.999%	ALDRICH - Nr 26,657-4
6	^{27}Al(A,B,D,E)	Al-99.96%	MS&GC Lab. No. 310-00/1
7	^{27}Al(S)	Al-99.999%	ALDRICH - Nr 26,657-4
8	^{27}Al(L,M,R,I,J,K)	Al-99.96%	MS&GC Lab. No. 310-00/2
9	^{59}Co	Co-98.5%,Ni-0.3%,Cu-0.2%, Zn-0.4%, other-0.15%	MS&GC Lab. No. 6961.98
10	^{63}Cu	^{63}Cu-99.46%,^{65}Cu-0.50%	Stable Isotope Research Center, No. 93-5
11	^{64}Zn	^{64}Zn-99.3%, ^{66}Zn-0.39%,	Kurchatov Atomic Energy Institute, State Center of Stable Isotopes, No. 197
12	^{65}Cu	^{65}Cu-99.665%, ^{63}Cu-0.30%	Stable Isotope Research Center, No. 99-12
13	^{93}Nb	Nb-99.99%	Science-Production Center, All-Russia Institute for Physical-Technical and Radio Measurements
14	^{115}In	^{115}In-99.98%	Kurchatov Atomic Energy Institute, State Center of Stable Isotopes, No. 98
15	^{169}Tm	Tm-99.9%	ACROS – Nr 31779-0010
16	^{181}Ta	Extremely pure	
17	^{197}Au	Extremely pure	
18	^{209}Bi	Bi-99.99%	ALDRICH – Nr 26,400-8

1.4 Monitoring of proton beam

The number of protons that hit the target and the proton beam shape were determined using an Al monitor placed in the beam at 5 cm before the first disc. After irradiation, the monitor was cut into fragments, mostly 2×2 cm squares. Fig. 6 is the monitor cut chart. The numbers of ^{7}Be, ^{22}Na, and ^{24}Na product nuclei in each fragment were determined by γ-spectrometric analysis. Since the number of the ^{7}Be product nuclei in each of the fragments is proportional to the number of protons that passed through a fragment[2], the results make it possible to determine the number of protons that passed through each of the fragments (see Table 6), whereupon the proton beam shape can readily be restored.

The $^{27}Al(p,x)^{7}Be$ reaction cross section for 0.8 GeV projectile proton energy was measured using thin Al targets in a number of irradiation runs under the ISTC Project #839B [1]. The $^{27}Al(p,x)^{22}Na$ reaction was used to monitor the irradiations. With the $^{27}Al(p,x)^{22}Na$ monitor reaction cross section 15.5±0.9 mbarn obtained from the data of [2], the $^{27}Al(p,x)^{7}Be$ reaction cross section was found to be 6.4±0.4 mbarn [3].

[2]Contrary to ^{7}Be, the ^{22}Na and ^{24}Na nuclei can also be produced due to neutrons ejected backwards from the target.

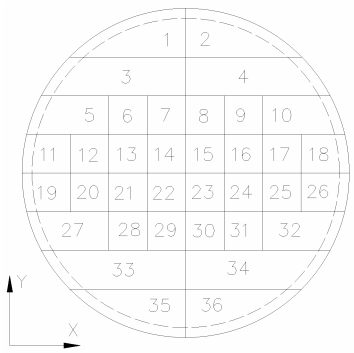

Fig. 6. The monitor cut chart.

Table 6. Results of determining the number of protons that hit the W-Na target.

Nos. of samples in Fig. 6	Mass, g	Reaction rate, $\left[10^{-20}\frac{1}{s\cdot nucleus\cdot W}\right]$	Number of protons that passed through a fragment, 10^{12}
27,32	2.699	0.84±0.20	1.8±0.4
33,34,35,36	7.820	0.42±0.05	2.5±0.3
5,6,7,8,9,10	5.330	1.38±0.11	5.7±0.4
1,2,3,4	8.163	0.48±0.04	3.0±0.3
12	0.696	9.5±1.1	5.1±0.6
13	0.684	9.7±1.1	5.1±0.6
14	0.676	129±9	68±5
15	0.668	297±19	153±10
16	0.690	111±7	59±4
17	0.680	15.2±1.4	8.0±0.7
18	0.815	6.4±0.8	4.0±0.5
21	0.685	5.0±1.0	2.6±0.5
22	0.683	108±8	57±4
23	0.681	318±21	167±11
24	0.698	158±11	85±6
25	0.683	24.2±1.9	12.8±1.0
26	0.830	9.7±0.9	6.2±0.6
29	0.703	3.8±0.8	2.1±0.4
30	0.694	3.1±0.8	1.6±0.4
Total number of proton projectiles = 651 ± 41			

Since the monitor fragments are fairly large (a smaller size involve a great error of count rate in the total absorption peak), the beam shape was restored by least squares method on assumption that the beam shape along either of the coordinates *x, y* is Gaussian-distributed. In this case the number, N_p, of protons that hit the i-th fragment is determined as

$$N_{p_i}(\vec{P}) = \iint\limits_{S_i} \frac{P_5}{2\pi P_2 P_4} e^{-\frac{(x-P_1)^2}{2P_2^2}} e^{-\frac{(y-P_3)^2}{2P_4^2}} dxdy \qquad (1)$$

where $(\vec{P}) = \{P_1, P_2, P_3, P_4, P_5,\}$ is the vector of the input parameters; S_i is the surface of the i-th fragment.

The parameters of $(\vec{P})$ are determined from the minimum of the functional

$$R = \sum_{i=1}^{N} \frac{1}{\sigma^2_{\tilde{N}_{p_i}}} \cdot \left(\tilde{N}_{p_i} - \frac{P_5}{2\pi P_2 P_4} \cdot \iint_{S_i} e^{-\frac{(x-P_1)^2}{2P_2^2}} e^{-\frac{(y-P_3)^2}{2P_4^2}} dxdy \right)^2 \qquad (2)$$

where $\sigma_{\tilde{N}_{pi}}$ is the error in $\tilde{N}_{p_i}$; N is the number of the monitor fragments.

Since the parameters of $(\vec{P})$ enter the function (1) nonlinearly, they were determined by iterations. With that purpose, the approximation function (1) was Taylor-series-expanded near the point $(\vec{P}_0)$ which is the zero approximation of the parameters $(\vec{P}_0)$. Minimizing the expression

$$R_i = \sum_{i=1}^{N} \frac{1}{\sigma^2_{\tilde{N}_{p_i}}} \cdot \left(\tilde{N}_{p_i} - \tilde{N}_{p_i}(\vec{P}_0) - \sum_{j=1}^{5} \left. \frac{\partial N_{p_i}}{\partial P_j} \right|_{\vec{P}=\vec{P}_0} \cdot \Delta P_j \right)^2 , \qquad (3)$$

we find the addends $\Delta\vec{P}$ to the parameters $\vec{P}$ from the conditions

$$\frac{\partial R_1}{\partial P_k} = 0 \qquad \text{k = 1, 2, 3, 4, 5 ,}$$

giving the ordinary set of linear equations with unknown addends $\Delta\vec{P}$ to the parameters $\vec{P}$:

$$M \cdot \Delta\vec{P} = \vec{b}$$

where

$$M_{ij} = \sum_{k=1}^{N} \frac{1}{\sigma^2_{\tilde{N}_{pk}}} \cdot \left. \frac{\partial N_{p_k}}{\partial P_i} \right|_{\vec{P}=\vec{P}_0} \left. \frac{\partial N_{p_k}}{\partial P_j} \right|_{\vec{P}=\vec{P}_0}$$

$$b_i = \sum_{k=1}^{N} \frac{1}{\sigma^2_{\tilde{N}_{pk}}} \cdot \left(\tilde{N}_{p_k} - \tilde{N}_{p_k}(\vec{P}_0) \right) \left. \frac{\partial N_{p_k}}{\partial P_i} \right|_{\vec{P}=\vec{P}_0}$$

After that, the above procedure is repeated near the point $\vec{P}_1 = \vec{P}_0 + \Delta\vec{P}$, etc. The iteration process stops when the condition $\left|\Delta\vec{P}\right| << \sigma_{p_i}$ is satisfied for all parameters (σ_{p_i} is the error in determining the parameter P_i.

Table 7 presents the results of determining the proton beam shape.

Table 7. Target irradiation parameters.

Parameter	Value
Proton number	$(6.51 \pm 0.41)\cdot 10^{14}$
Beam shape parameters, cm	
P_1	1.12
P_2	1.557
P_3	0.02
P_4	0.981

1.5 Determination of reaction rates

The reaction rates were determined by the high-precision γ-spectrometry techniques described in Subsection 1.9.1 above.

2 Experimental results

2.1 Normalization of experimental data

The proton beam power during the irradiation can be described as

$$W = \frac{N}{T} \cdot E,$$

where E is the proton beam energy (800 MeV);

N is the total number of protons that hit the target within the irradiation time ($(6.51 \pm 0.41) \times 10^{14}$);

T is the total irradiation time (35 952 s).

Considering the values of the parameters N, E, and T, the resultant power is

$$W = (2.32 \pm 0.15)\,\text{W}.$$

Since the experimental reaction rates have the dimension $\left[\frac{1}{s}\right]$, they can be renormalizes as $\left[\frac{1}{s \times W}\right]$ after introducing the normalization $R_{norm}^{\exp} = \frac{R^{\exp}}{W}$. In the LAHET code system, the density of the particle flux produced by a single proton-target interaction event is expressed in units of $\left[\frac{1}{cm^2}\right]$. Therefore, the calculated reaction rate $R^{calc} = \int_0^{\infty} \sigma(E) \cdot \phi(E) dE$ is dimensionless. Introducing the normalization $R_{norm}^{calc} = \frac{R^{calc}}{E}$, we can also renormalize the calculated reaction rates to the form $\left[\frac{1}{s \times W}\right]$. In this case, the normalization factor for $E_p = 0.8$ GeV is

$$K = 0.8 \cdot 10^9 [eV] \times 1.60206 \cdot 10^{-19} \left[J/_{eV}\right] = 1.2816 \cdot 10^{-10} [J] = 1.2816 \cdot 10^{-10} [s \cdot W].$$

Tables 8-22 present the results of experimental determining the rates residual nuclide production in ^{209}Bi, ^{197}Au, ^{169}Tm, ^{115}In, ^{93}Nb, ^{65}Cu, ^{64}Zn, ^{63}Cu, ^{59}Co, ^{27}Al, ^{19}F, and ^{12}C. Table 23 presents the total number of the reactions scheduled and actually measured.

Table 8. Rates of residual nuclide production in ^{209}Bi on the W-Na target surface, $\left[10^{-20}\ \frac{1}{s \cdot nucleus \cdot W}\right]$.

Nuclide	$T_{1/2}$	Yield type	L, cm									
			1.4	15	25	35	42	50	58	66	74	84.7
^{207}Po	5.80h	i(m+g)	1.40±0.49	7.24±0.75	6.94±0.68	7.93±0.99	5.04±0.50	4.35±0.62	3.74±0.47	0.854±0.125		
^{206}Po	8.8d	i	1.60±0.23	7.76±0.52	8.15±0.61	8.23±0.67	4.96±0.34	4.40±0.42	4.48±0.34	0.996±0.225		
^{206}Bi	6.243d	i	68.1±4.4	128±8	138±9	127±8	117±8	89.7±6.0	57.3±3.7	24.6±1.6	11.0±0.8	4.17±0.29
^{206}Bi	6.243d	c	69.0±4.5	134±9	145±10	134±9	122±8	93.6±6.2	61.6±4.1	25.1±1.6	11.5±0.8	4.40±0.29
^{205}Bi	15.31d	c	52.2±4.2	113±8	122±9	113±8	101±7	79.3±5.5	54.3±4.1	21.0±1.8	10.2±1.1	4.57±1.17
^{204}Bi	11.22h	c	28.8±2.2	69.8±5.3	77.6±5.9	75.0±5.7	64.7±4.9	50.4±4.0	36.2±2.8	12.8±1.1	6.08±0.48	2.39±0.21
^{203}Bi	11.76h	c	21.1±1.5	53.5±3.8	59.9±4.2	59.1±4.2	50.0±3.5	41.6±3.4	30.1±2.4	10.3±0.8	5.30±0.42	1.77±0.17
^{203}Pb	51.873h	i	7.80±1.44	20.4±3.0	23.7±3.3	27.1±4.5	17.2±1.4	20.4±2.2	10.1±1.5	5.65±0.76	2.51±0.57	1.40±0.26
^{203}Pb	51.873h	c	31.6±2.2	82.3±5.8	93.6±6.6	89.7±6.4	75.0±5.3	61.2±4.3	44.4±3.1	16.1±1.1	7.76±0.56	3.18±0.23
^{201}Pb	9.33h	c*	14.7±1.8	53.5±4.3	59.1±5.6	62.1±4.9	47.9±4.0	39.0±3.4	31.4±2.6	10.4±0.8	5.17±0.43	2.02±0.21
^{200}Pb	21.5h	c	8.62±0.99	33.5±3.0	38.8±3.5	37.3±3.4	32.2±3.0	24.4±2.6	20.7±1.8	6.04±1.03	2.86±0.36	1.09±0.10
^{202}Tl	12.23d	i*	1.98±0.15	5.13±0.46	5.60±0.47	5.39±0.39	4.57±0.32	3.55±0.26	2.31±0.18	1.04±0.12	0.556±0.061	0.277±0.041
^{200}Tl	26.1h	i(m+g)	3.23±0.97	5.69±1.09	7.80±1.14	7.93±1.52	3.06±1.50	5.99±2.20	2.75±0.52	1.89±1.23	0.767±0.321	0.573±0.052
^{200}Tl	26.1h	c	11.9±1.1	39.2±3.5	46.6±4.1	45.3±4.1	35.3±3.2	30.4±2.9	23.5±2.1	7.93±0.95	3.63±0.37	1.66±0.15
^{191}Pt	2.802d	i(m)	3.24±0.80	6.68±0.94	7.59±1.10	7.16±1.25	6.47±1.06	4.22±0.77				
^{96}Tc	4.28d	i(m+g)		0.351±0.116	0.348±0.164	0.599±0.088	0.241±0.089					
^{96}Nb	23.35h	i		0.854±0.176	0.944±0.272	0.664±0.139	1.22±0.17	0.776±0.106	0.612±0.125			
^{82}Br	35.30h	i(m+g)		0.763±0.100	0.810±0.110	0.612±0.098	0.703±0.123	0.664±0.309				

Table 9. Rates of residual nuclide production in ^{197}Au on the W-Na target surface, $\left[10^{-20}\ \frac{1}{s \cdot nucleus \cdot W}\right]$.

Nuclide	$T_{1/2}$	Yield type	L, cm									
			1.4	15	25	35	42	50	58	66	74	84.7
^{198}Au	2.69517d	i†	729±46	831±53	869±55	979±62	1076±68	989±63	845±54	773±49	699±44	531±34
^{196}Au	6.183d	$i(m_1+m_2+g)$	269±17	431±28	435±28	401±26	347±22	257±18	151±10	62.9±4.2	28.6±2.2	10.1±3.1
^{194}Au	38.02h	$i(m_1+m_2+g)$	77.4±8.2	149±16	156±16	150±16	123±13	102±11	64.2±6.9	33.8±4.0	13.4±1.9	
^{191}Pt	2.802d	c		82.0±17.0	89.2±13.2	70.2±11.9	71.1±11.8					

† The 198mAu γ-line is absent from the spectra.- В гамма-спектрах нет линии 198mAu.

Table 10. Rates of residual nuclide production in ^{115}In on the W-Na target surface, $\left[10^{-20}\,\frac{1}{s\cdot nucleus\cdot W}\right]$.

Nuclide	$T_{1/2}$	Yield type	L, cm									
			1.4	15	25	35	42	50	58	66	74	84.7
^{113}Sn	115.09d	i(m+g)	3.57±0.26	6.27±1.09	9.56±0.94	9.81±0.97	5.62±0.51	4.48±0.50	4.55±0.50			
^{116}In	54.29m	i(m_1+m_2)	620±41	790±52	806±54	869±61	923±65	728±49	486±32	304±22	224±15	164±11
^{115}In	4.486h	i(m)	376±30	551±44	567±46	548±44	506±41	370±30	203±16	77.0±6.2	33.0±2.7	
^{115}In	4.486h	c	377±30	553±45	569±46	549±44	508±41	371±30	204±16	77.7±6.3	33.5±2.7	14.1±1.2
^{114}In	49.51d	i(m_1+m_2)	180±12	282±19	297±20	272±19	245±17	180±12	108±7	42.9±3.0	18.9±1.6	7.60±0.67
^{113}In	99.476m	i(m)†	9.28±0.63	16.9±1.9	19.1±1.7	16.4±1.6	15.4±1.3	11.0±1.2	7.07±0.78			
^{113}In	99.476m	c	12.9±0.9	23.1±2.4	28.7±2.3	26.2±2.2	21.0±1.7	15.4±1.4	11.6±1.1	3.25±0.33	1.33±0.19	
^{111}In	2.8047d	c	25.5±1.7	58.5±3.8	65.9±4.3	60.3±4.0	53.0±3.5	42.5±2.8	30.9±2.0	10.6±0.7	5.07±0.34	1.91±0.13
^{110}In	4.9h	i	7.75±0.60	19.6±1.5	22.6±1.5	20.2±1.4	18.2±1.3	15.0±1.0	11.2±0.8	3.65±0.31	1.77±0.16	0.658±0.084
^{109}In	4.2h	c	5.58±0.42	16.4±1.2	19.0±1.3	18.2±1.3	15.6±1.1	12.1±0.9	10.4±0.7	2.64±0.22	1.28±0.13	0.649±0.132
^{115}Cd	53.46h	c	1.01±0.10	2.47±0.25	2.80±0.25	1.83±0.18	2.28±0.23	1.51±0.61	0.942±0.096	0.709±0.058		
^{111}Ag	7.45d	c	3.14±0.53	4.60±0.73	6.06±0.81	4.93±0.74	5.58±1.48	4.47±0.73				
^{110}Ag	249.76d	i(m)		4.83±0.80	4.03±1.10	5.45±1.07	3.39±0.71					
^{106}Ag	8.28d	i(m)	2.56±0.22	7.62±0.52	8.75±0.59	8.54±0.59	6.97±0.51	5.85±0.41	4.31±0.31	1.64±0.31		
^{105}Ag	41.29d	c	3.64±0.31	13.0±1.1	16.4±1.2	16.8±1.2	12.5±0.9	10.6±0.9	8.31±0.62	2.15±0.23		
^{101}Pd	8.47h	c	1.93±0.37	4.57±0.56	3.91±0.58	5.60±0.77	4.14±0.50	2.16±0.50				
^{100}Pd	3.63d	c	0.558±0.058	1.77±0.17	2.63±0.32	2.27±0.17	1.90±0.15	1.43±0.11	0.882±0.064	0.299±0.022		
^{101}Rh	4.34d	c	2.32±0.24	7.39±0.68	9.35±0.85	9.20±0.84	7.20±0.65	5.27±0.48	3.68±0.34	1.06±0.11		
^{100}Rh	20.8h	i(m+g)	1.15±0.10	3.79±0.31	3.61±0.30	4.61±0.30	2.84±0.32	2.27±0.19	1.53±0.11	0.423±0.031		
^{100}Rh	20.8h	c	1.71±0.13	5.35±0.48	6.24±0.43	6.88±0.45	4.73±0.42	3.70±0.26	2.41±0.16	0.722±0.049		
^{99}Rh	4.7h	c			3.56±0.48	3.84±0.43		2.15±0.29	1.18±0.17	0.587±0.130		
^{97}Ru	2.791d	c	1.19±0.10	3.13±0.23	3.91±0.27	4.07±0.30	2.98±0.21	2.18±0.16	1.11±0.09	0.343±0.047	0.271±0.038	
^{96}Tc	4.28d	i(m+g)	0.511±0.058	1.28±0.10	1.65±0.16	1.63±0.12	1.22±0.11	0.731±0.065				
^{95}Tc	20.0h	c	0.942±0.107	2.22±0.17	2.88±0.25	2.85±0.21	2.07±0.18	1.33±0.12	0.886±0.093			
^{90}Mo	5.56h	c		0.430±0.093		0.795±0.178						
^{90}Nb	14.60h	i(m_1+m_2+g)		0.414±0.122	0.854±0.198							
^{90}Nb	14.60h	c	0.443±0.038	0.845±0.067	1.00±0.09	0.839±0.085						
^{89}Zr	78.41h	c	0.934±0.112	1.12±0.19	1.28±0.11	1.35±0.13						
^{87}Y	79.8h	c	0.466±0.048	0.717±0.100	0.910±0.082	0.630±0.104						

† The 113mSn contribution is disregarded because it is ≤10%.

Table 11. Rates of residual nuclide production in ^{181}Ta on the W-Na target surface, $\left[10^{-20}\ \frac{1}{s \cdot nucleus \cdot W}\right]$.

Nuclide	$T_{1/2}$	Yield type	L, cm									
			1.4	15	25	35	42	50	58	66	74	84.7
^{182}Ta	114.43d	i(m_1+m_2+g)	745±63	928±67	929±67	904±80	1038±74	842±64	649±47	414±35	310±42	251±34
^{178}Ta	2.36h	i(m)	42.7±2.9	79.2±5.3	85.4±5.6	79.5±5.2	73.2±5.1	55.3±3.7	35.6±2.4	13.2±0.9	5.67±0.51	2.46±0.27
^{176}Ta	8.09h	c*	45.4±5.0	92.0±9.7	110±11	93.2±9.9	79.5±9.7	69.1±7.9	49.8±11.7	16.3±2.8		
^{175}Ta	10.5h	c	40.5±5.6	94.5±11.0	99.5±11.5	93.5±11.1	82.1±11.4	65.3±8.0	55.0±7.0	13.2±4.0		
^{173}Ta	3.14h	c	16.8±2.5	27.3±3.9	31.3±5.3	38.0±5.8	24.1±3.7	24.6±3.7	23.2±5.7			
^{180}Hf	5.5h	i(m)	1.65±0.31	4.87±0.72	4.15±0.46	3.57±0.43	4.31±0.82	2.05±0.47	1.12±0.68	1.65±0.48		
^{175}Hf	70d	c	34.4±3.8	88.0±7.6	106±9	97.4±9.6	80.8±7.7	62.7±6.0	47.2±4.6	14.6±5.8		
^{173}Hf	23.6h	c*	21.7±1.8	62.6±4.4	80.7±5.6	73.2±5.2	56.9±4.0	50.7±3.9	44.7±3.5	14.7±1.2	7.22±0.75	2.47±0.36
^{170}Hf	16.01h	c	11.7±3.8	30.6±5.2	38.5±6.6	32.6±5.5	24.9±4.4	25.8±4.7	21.8±4.4			
^{172}Lu	6.70d	i(m+g)		7.49±1.42	7.29±1.49							
^{171}Lu	8.24d	c	10.9±3.4	34.2±2.8	39.4±4.0	43.7±6.7	32.7±5.6	32.4±2.8	26.2±2.4			
^{169}Lu	34.06h	c		19.5±2.6	23.4±2.3	23.2±2.0	20.3±2.5	17.1±1.7	17.6±1.9			
^{167}Tm	9.25d	c	5.19±1.40	24.3±5.2	25.2±5.2	25.4±6.0	21.1±4.6	19.0±4.1	12.3±2.7	7.65±4.86		
^{165}Tm	30.06h	c	6.02±2.18	12.9±1.5	17.6±1.6	16.5±1.5	13.2±1.3	12.1±1.2	7.12±1.25	3.31±0.68		
^{161}Er	3.21h	c*		6.59±1.40	9.76±1.68	10.4±1.7	8.72±1.53	5.07±1.20				

Table 12. Rates of residual nuclide production in ^{59}Co inside the W-Na target, $\left[10^{-20}\,\frac{1}{s\cdot nucleus\cdot W}\right]$.

Nuclide	$T_{1/2}$	Yield type	L, cm									
			0	14	24	34	40	48	56	64	72	82.7
^{57}Ni	35.60h	i	22.7±3.0	22.8±2.7	13.8±1.8	6.98±0.61	4.61±0.44					
^{58}Co	9.04h	i(m)	7070±793	3962±270	3126±255	1444±155	798±130	655±64	221±27	125±9		
^{58m}Co	70.86d	i	3134±684	2906±207	785±165	556±129	638±127	67.7±47.6	120±24	55.6±5.1		
^{58}Co	70.86d	i(m+g)	10217±658	6855±441	3910±252	2000±129	1436±92	724±47	341±22	181±12	23.3±1.6	8.06±0.55
^{57}Co	271.74d	c	4199±271	2914±188	1686±109	854±55	604±39	314±20	163±11	122±8	8.71±0.63	3.30±0.28
^{56}Co	77.233d	c	927±60	638±41	377±24	189±12	131±8	70.3±4.5	39.8±2.8	27.8±2.0	1.77±0.18	0.668±0.085
^{55}Co	17.53h	c	121±9	90.1±6.8	49.6±3.9	25.9±2.0	16.1±1.7	10.3±1.1	5.60±0.54	2.25±0.33		
^{59}Fe	44.472d	c	724±49	487±33	286±20	153±11	120±8	60.8±4.2	25.7±1.9	7.46±0.79	2.75±0.25	1.00±0.16
^{52}Fe	8.275h	c	17.4±2.3	13.0±1.3	8.45±0.83	3.63±0.39	2.30±0.33	1.13±0.13	0.729±0.092			
^{56}Mn	2.5789h	c	961±68	595±41	342±24	169±13	113±9	55.6±4.6	24.8±2.1	8.19±0.87	1.71±0.37	0.616±0.148
^{52}Mn	5.591d	c	1095±71	716±46	401±26	196±13	126±8	60.4±4.2	28.7±1.9	5.48±0.52		
^{51}Cr	27.7025d	c	3798±248	2401±157	1341±88	660±44	416±27	195±13	86.7±6.0	10.2±1.6	2.82±0.50	0.979±0.221
^{48}Cr	21.56h	c	54.8±3.7	33.5±2.6	18.5±1.3	8.54±0.61	5.43±0.42	2.33±0.23	0.879±0.110			
^{48}V	15.9735d	c	1802±115	1117±71	599±38	278±18	171±11	70.7±4.6	26.1±1.7	1.40±0.19	0.368±0.076	0.157±0.024
^{48}Sc	43.67h	i	86.2±6.1	51.7±4.2	26.6±1.9	11.5±0.9	6.68±0.64	2.83±0.42	0.897±0.301			
^{47}Sc	3.3492d	c	440±29	260±17	138±9	61.2±4.0	36.8±2.6	13.6±0.9				
^{47}Sc	3.3492d	i		268±18	141±9	62.5±4.1	37.4±2.6	14.2±1.0	4.44±0.36			
^{46}Sc	83.79d	i(m+g)	1091±70	655±43	342±22	152±11	89.2±5.8	35.9±3.0	10.5±1.2	4.44±0.39	3.52±0.30	1.89±0.17
^{44m}Sc	58.61h	i(m)	828±57	487±35	246±17	111±8	62.1±4.0	20.4±1.4	5.48±0.39			
^{44}Sc	3.97h	i(m+g)	785±54	440±32	229±15	89.7±6.2	54.3±3.5	20.5±1.3	4.35±0.28			
^{44}Sc	3.97h	i	1587±104	910±61	470±31	197±13	115±7	40.4±2.6	9.74±0.63			
^{43}Sc	3.891h	c	429±50	268±28	107±17	53.5±5.6	29.4±4.5	6.55±2.11	1.07±1.21			
^{47}Ca	4.536d	c	9.36±0.75	6.94±0.54	3.34±0.25	1.21±0.16	0.634±0.635	0.681±0.123				
^{43}K	22.3h	c	161±10	91.8±6.1	44.4±2.9	17.3±1.2	10.4±0.7	3.68±0.33	0.948±0.171			
^{24}Na	14.9590h	c	103±7	48.7±3.4	20.1±1.6	7.89±1.27	3.97±0.39					
^{7}Be	53.29d	i	310±30	165±13	83.2±9.7							

Table 13. Rates of residual nuclide production in ^{27}Al on the W-Na target surface, $\left[10^{-20}\,\frac{1}{s\cdot nucleus\cdot W}\right]$.

	Nuclide	$T_{1/2}$	Yield type	L, cm									
				1.4	15	25	35	42	50	58	66	74	84.7
S	^{27}Mg	9.458m	i	22.9±2.4	31.8±3.5	35.1±3.3	34.0±3.2	31.5±2.5	20.2±1.9	11.2±1.1	4.73±0.51	2.11±0.49	
S	^{24}Na	14.9590h	c	20.2±1.3	33.1±2.1	34.6±2.2	32.5±2.1	28.2±1.8	20.8±1.3	12.4±0.8	5.11±0.34	2.29±0.15	0.896±0.064
S	^{22}Na	2.6019y	c	3.00±0.34	7.58±0.72	9.13±0.75	9.29±0.80	7.46±0.68	5.05±0.56	3.90±0.51	1.14±0.33		
S	^{7}Be	53.29d	i			0.692±0.238	0.917±0.242	0.685±0.194	0.714±0.333	0.637±0.329			
L	^{24}Na	14.9590h	c	19.4±1.3		33.4±2.2		26.5±1.7		11.8±0.8			
L	^{22}Na	2.6019y	c	5.08±1.45		11.3±1.4		8.63±1.80		4.47±0.87			
M	^{24}Na	14.9590h	c	19.5±1.3		33.3±2.2		28.1±1.8		12.0±0.8			
M	^{22}Na	2.6019y	c	3.56±0.95		10.2±1.7		8.26±1.43		5.72±1.12			
R	^{24}Na	14.9590h	c	25.4±1.7		41.5±2.7		36.6±2.4		15.4±1.0			
R	^{22}Na	2.6019y	c	4.16±1.78		11.9±1.4		9.25±1.31		5.35±0.51			
I	^{22}Na	2.6019y	c	4.74±0.67		10.7±0.9		8.16±0.86		3.85±0.63			
J	^{22}Na	2.6019y	c	2.71±0.63		8.91±0.83		6.89±0.94		4.26±0.71			
K	^{22}Na	2.6019y	c	3.96±0.58		12.7±1.1		9.76±0.79		6.73±0.69			

Table 14. Rates of residual nuclide production in ^{27}Al inside the W-Na target, $\left[10^{-20}\,\frac{1}{s\cdot nucleus\cdot W}\right]$.

	Nuclide	$T_{1/2}$	Yield type	L,cm									
				0	14	24	34	40	48	56	64	72	82.7
A	^{24}Na	14.9590h	c	48.8±3.2	70.4±4.6	102±7	60.8±3.9	63.3±4.1	46.0±3.0	27.5±1.8	11.0±0.7	3.58±0.25	1.33±0.09
A	^{22}Na	2.6019y	c	11.8±2.9	22.6±3.6	19.5±2.9	19.9±2.6	21.5±2.0	15.8±2.5	14.7±1.8			
B	^{24}Na	14.9590h	c	249±16	240±16	236±16	162±11	153±10	90.1±5.8	45.8±3.0	16.0±1.0	4.21±0.30	1.51±0.10
B	^{22}Na	2.6019y	c	75.4±6.3	92.1±8.3	116±9	93.1±7.7	70.9±5.8	52.5±5.4	26.2±2.9	11.9±1.7		
B	^{7}Be	53.29d	i	20.8±2.5	23.8±3.4	24.7±3.1	22.6±3.6	15.9±3.3	10.3±4.0	3.48±2.68			
C	^{27}Mg	9.458m	i	2643±904	1608±546	745±251	317±39	256±35	141±18	58.2±9.8	21.0±4.6		
C	^{24}Na	14.9590h	c	2562±166	1576±102	873±58	436±29	307±20	145±9	63.7±4.1	18.2±1.2	4.33±0.31	1.51±0.10
C	^{22}Na	2.6019y	c	1834±124	1178±81	654±47	310±23	195±15	87.1±8.7	48.7±4.8	23.0±3.8		
C	^{7}Be	53.29d	i	676±45	401±28	187±15	76.8±6.4	41.5±4.1	22.8±4.8	15.7±3.8			
D	^{24}Na	14.9590h	c	331±22	406±26	393±26	305±20	240±16	133±9	59.4±3.9	16.5±1.1	4.24±0.29	1.33±0.09
D	^{22}Na	2.6019y	c	54.8±5.2	151±11	210±15	182±13	140±10	79.2±6.7	39.7±3.3	15.5±2.4		
D	^{7}Be	53.29d	i	15.7±2.6		57.4±5.0	49.6±5.0	28.2±3.9	18.3±3.8				
E	^{24}Na	14.9590h	c	78.1±5.1	112±7	112±7	104±7	109±7	75.4±4.9	40.6±2.6	12.9±0.9	3.65±0.25	1.31±0.09
E	^{22}Na	2.6019y	c	8.12±2.20	29.9±4.1	38.5±4.2	40.7±4.2	44.8±3.9	39.2±3.9	24.3±2.9			
E	^{7}Be	53.29d	i		12.1±5.8		16.8±4.9	13.0±5.0					

Table 15. Rates of residual nuclide production in ^{59}Co on the second disc on the W-Na target surface, $\left[10^{-20}\ \frac{1}{s \cdot nucleus \cdot W}\right]$.

Nuclide	$T_{1/2}$	Yield type	R ± ΔR
^{57}Ni	35.60h	i	0.336±0.041
^{60}Co	5.2714y	i	55.1±4.9
^{58}Co	9.04h	i(m)	100±6
^{58}Co	70.86d	i	51.0±3.3
^{58}Co	70.86d	i(m+g)	151±10
^{57}Co	271.74d	c	51.9±3.6
^{56}Co	77.233d	c	7.91±0.53
^{55}Co	17.53h	c	0.776±0.080
^{59}Fe	44.472d	c	16.5±1.2
^{52}Fe	8.275h	c	0.057±0.009
^{56}Mn	2.5789h	c	10.3±0.7
^{52}Mn	5.591d	c	3.66±0.25
^{51}Cr	27.7025d	c	10.2±0.8
^{48}Cr	21.56h	c	0.092±0.010
^{48}V	15.9735d	c	2.95±0.22
^{48}Sc	43.67h	i	0.12±0.04
^{47}Sc	3.3492d	i	0.702±0.047
^{47}Sc	3.3492d	c	0.735±0.049
^{46}Sc	83.79d	i(m+g)	1.58±0.22
^{44m}Sc	58.61h	i(m)	0.943±0.061
^{44}Sc	3.97h	i	0.458±0.030
^{44}Sc	3.97h	i(m+g)	1.39±0.09
^{47}Ca	4.536d	c	0.033±0.002

Table 16. Rates of residual nuclide production in ^{65}Cu on the second disc on the W-Na target surface, $\left[10^{-20}\ \frac{1}{s \cdot nucleus \cdot W}\right]$.

Nuclide	$T_{1/2}$	Yield type	R ± ΔR
^{64}Cu	12.700h	i	242±16
^{61}Cu	3.333h	c	7.29±0.92
^{65}Ni	2.5172h	i	9.55±0.75
^{58}Co	70.86d	i(m+g)	16.6±2.3
^{57}Co	271.74d	c	11.2±3.1
^{56}Co	77.233d	c	3.11±1.09
^{55}Co	17.53h	c	0.240±0.041
^{56}Mn	2.5789h	c	2.38±0.17
^{52}Mn	5.591d	c	1.07±0.10
^{44m}Sc	58.61h	i(m)	0.303±0.027
^{44}Sc	3.97h	i	0.147±0.016
^{44}Sc	3.97h	i(m+g)	0.446±0.034

Table 17. Rates of residual nuclide production in ^{64}Zn on the second disc on the W-Na target surface, $\left[10^{-20}\ \frac{1}{s \cdot nucleus \cdot W}\right]$.

Nuclide	$T_{1/2}$	Yield type	R ± ΔR
^{65}Zn	244.26d	i	72.3±8.6
^{63}Zn	38.47m	c	100±7
^{62}Zn	9.186h	c	12.5±1.0
^{64}Cu	12.700h	i	185±14
^{61}Cu	3.333h	c	32.3±3.7
^{60}Cu	23.7m	c	8.18±0.71
^{57}Ni	35.60h	c	1.15±0.10
^{58}Co	70.86d	i(m+g)	21.3±1.9
^{57}Co	271.74d	c	21.9±3.7
^{56}Co	77.233d	c	7.28±0.84
^{55}Co	17.53h	c	1.04±0.09
^{56}Mn	2.5789h	c	0.660±0.052
^{52}Mn	5.591d	c	2.66±0.19
^{48}Cr	21.56h	c	0.096±0.044
^{44m}Sc	58.61h	i(m)	0.468±0.048
^{44}Sc	3.97h	i	0.348±0.035
^{44}Sc	3.97h	i(m+g)	0.780±0.073

Table 18. Rates of residual nuclide production in ^{19}F on the second disc on the W-Na target surface, $\left[10^{-20}\ \frac{1}{s \cdot nucleus \cdot W}\right]$.

Nuclide	$T_{1/2}$	Yield type	R ± ΔR
^{18}F	109.77m	c	15.6±0.7

Table 19. Rates of residual nuclide production in ^{63}Cu on the second disc on the W-Na target surface, $\left[10^{-20}\ \frac{1}{s \cdot nucleus \cdot W}\right]$.

Нуклид	$T_{1/2}$	Yield type	R ± ΔR
^{61}Cu	3.333h	c	36.8±4.2
^{58}Co	70.86d	i(m+g)	27.4±3.3
^{55}Co	17.53h	c	0.773±0.133
^{52}Mn	5.591d	c	2.76±0.24

Table 20. Rates of residual nuclide production in ^{12}C on the second disc on the W-Na target surface, $\left[10^{-20}\ \frac{1}{s \cdot nucleus \cdot W}\right]$.

Nuclide	$T_{1/2}$	Yield type	R ± ΔR
^{11}C	20.39m	i	28.0±2.2

Table 21. Rates of residual nuclide production in ^{93}Nb on the second disc on the W-Na target surface, $\left[10^{-20}\ \frac{1}{s \cdot nucleus \cdot W}\right]$.

Nuclide	$T_{1/2}$	Yield type	R ± ΔR
^{90}Nb	14.60h	c	37.2±2.5
^{89}Zr	78.41h	c	42.5±2.9
^{86}Zr	16.5h	c	3.54±0.25
^{90}Y	3.19h	i	2.66±0.35
^{87}Y	13.37h	c *	24.0±1.6
^{87}Y	79.8h	c *	25.2±2.0
^{86}Y	14.74h	i(m+g)	9.7±0.68
^{86}Y	14.74h	c	13.4±0.9

Table 22. Rates of residual nuclide production in ^{169}Tm on the second disc on the W-Na target surface, $\left[10^{-20}\ \frac{1}{s \cdot nucleus \cdot W}\right]$.

Nuclide	$T_{1/2}$	Yield type	R ± ΔR
^{166}Yb	56.7h	i	17.0±2.8
^{168}Tm	93.1d	i	336±27
^{167}Tm	9.25d	c	215±44
^{166}Tm	7.70h	i	108±7
^{166}Tm	7.70h	c	121±8
^{165}Tm	30.0h	c	91.3±7.0
^{163}Tm	1.810h	c*	45.6±3.8
^{161}Er	3.21h	c*	38.1±3.8
^{160}Er	28.58h	c	26.4±3.0
^{160m}Ho	5.02h	i(m)	2.99±0.52
^{160}Ho	5.02h	c	29.2±3.3
^{157}Dy	8.14h	c	18.8±1.5
^{155}Dy	9.9h	c*	12.4±1.0
^{153}Dy	6.4h	c	6.92±0.99
^{152}Dy	2.38h	c	5.67±0.55
^{153}Tb	2.34d	c*	11.2±1.1
^{152}Tb	17.5h	c*	7.32±0.68
^{151}Tb	17.609h	c	5.23±0.41
^{150}Tb	3.48h	c	2.00±0.43

Table 23. List of the reactions scheduled and actually measured.

Reactions scheduled	No. of a respective Table; cumulative yield type	Number of reaction types measured additionally	Total number of the reaction types measured	Total number of the reaction rates presented	Number of the reactions planned to present
$^{209}Bi(n,7n)^{203}Bi$	8, (c)	13	18	157	24
$^{209}Bi(n,6n)^{204}Bi$	8, (c)				
$^{209}Bi(n,5n)^{205}Bi$	8, (c)				
$^{209}Bi(n,4n)^{206}Bi$	8, (i, c)				
$^{197}Au(n,4n)^{194}Au$	9,(i(m_1+m_2+g))	2	4	33	24
$^{197}Au(n,2n)^{196}Au$	9, (i(m_1+m_2+g))				
$^{115}In(n,5n)^{111}In$	10, (c)	24	29	207	30
$^{115}In(n,2n)^{114}In$	10, (i(m_1+m_2))				
$^{115}In(n,p)^{115}Cd$	10, c				
$^{115}In(n,n')^{115m}In$	10, (i(m), c)				
$^{182}Ta(n,x)$	11,-	15	15	112	-
$^{59}Co(n,2n)^{58}Co$	12, 15, i(m+g)	24	26	315	2
$^{59}Co(n,p)^{59}Fe$	12, 15,c				
$^{27}Al(n,p)^{27}Mg$	13, 14, i	2	4	184	24
$^{27}Al(n,a)^{24}Na$	13, 14, c				
$^{65}Cu(n,2n)^{64}Cu$	16, c	11	12	12	1
$^{64}Zn(n,2n)^{63}Zn$	17, c	15	17	17	2
$^{64}Zn(n,p)^{64}Cu$	17, c				
$^{19}F(n,2n)^{18}F$	18, c	-	1	1	1
$^{63}Cu(n,3n)^{61}Cu$	19, c	3	4	4	1
$^{12}C(n,2n)^{11}C$	20, c	-	1	1	1
$^{93}Nb(n,4n)^{90}Nb$	21, c	7	8	8	1
$^{169}Tm(n,4n)^{166}Tm$	22, c	18	19	19	1
Total					
	24	134	158	1070	112

3 Simulation of the measured reaction rates

Reaction rates were simulated using

1. the LCS code system [4], which includes

- ◊ the LAHET code to simulate the high-energy (E_n>20 MeV) hadron-nucleus interactions and;
- ◊ the HMCNP code to simulate the slow (E_n<20 MeV) neutron transport in matter.

The LAHET code allows for multiple scattering of primary protons and for elastic scattering of >20 MeV neutrons. The proton beam parameters are taken to agree with the results of determining the proton shape in Subsection 2.1.4 . The hadron-nucleus interactions were simulated in terms of the ISABEL model. The HMCNP code used the neutron cross sections retrieved from the ENDF/B-V database.

On using the LSC code system, we have obtained the neutron spectra in the locations of the experimental samples;

2. the package of nuclear databases with the cross sections of the reactions measured, which includes

- o the MENDL2 [5] cross section database of the up-to 100 MeV proton-induced reactions;
- o the MENDL2P [6] cross section database of the up-to 200 MeV proton-induced reactions.

In case the high-energy range (100-800 MeV), which is missing from the above databases, may contribute much to the measured reaction rates (Al and Co inside the target), the cross sections retrieved from the databases were supplemented with the well-known experimental cross sections (EXFOR).

The sought reaction rates were obtained via multiplication of the spectra by the respective reaction rates:

$$R = R_{n,x} + R_{p,x} = \sum_{i=n,p} \int \phi_i(E) \cdot \sigma_{i,x}(E) \cdot dE \quad . \tag{5}$$

The differences between the calculated and experimental reaction rates were estimated using the mean squared deviation factor <F>, see formula(40) sec. 1.14. Tables 24-26 show the simulated reaction rates. Fig. 7 shows both simulated and measured reaction rates.

Table 24. The simulated reaction rates along the S line of W-Na target, $\left[10^{-20}\,\frac{1}{s\cdot nucleus\cdot W}\right]$.

Nucleus	Product	L, cm									
		1.4	15	25	35	42	50	58	66	74	84.7
^{27}Al	^{27}Mg	37.11	54.68	58.03	55.72	49.50	33.74	19.45	9.348	3.609	0.9676
^{27}Al	^{24}Na	18.35	30.42	34.24	31.44	29.50	20.67	12.87	6.274	2.849	0.7688
^{197}Au	^{194}Au	71.59	119.5	123.8	112.5	103.4	77.40	49.24	23.56	7.477	1.885
^{197}Au	^{196}Au	268.0	387.5	421.0	369.9	365.0	248.1	139.3	78.02	35.87	9.356
^{209}Bi	^{203}Bi	23.26	53.04	53.55	48.56	46.45	34.95	31.74	10.27	3.593	0.7881
^{209}Bi	^{204}Bi	30.81	57.09	59.19	49.99	49.20	42.46	29.00	8.654	3.736	1.442
^{209}Bi	^{205}Bi	69.79	117.7	126.6	108.5	106.7	81.54	57.49	21.11	11.99	4.516
^{209}Bi	^{206}Bi	84.58	141.8	145.4	133.0	123.9	95.27	60.25	27.93	9.340	2.428
^{115}In	^{115}Cd	8.794	13.70	14.19	13.05	12.70	9.153	5.626	2.793	1.393	0.372
^{115}In	^{111}In	35.36	63.52	67.04	56.64	56.62	46.20	32.52	10.08	5.238	2.227
^{115}In	^{114}In	224.5	328.4	357.1	307.1	308.5	214.3	125.0	67.25	31.67	8.560

Table 25. The simulated reaction rates along the C line of W-Na target, $\left[10^{-20}\,\frac{1}{s\cdot nucleus\cdot W}\right]$.

Nucleus	Product	L, cm									
		0	14	24	34	40	48	56	64	72	82.7
^{27}Al	^{27}Mg	1402	984.7	659.6	374.3	300.8	154.3	66.26	21.95	6.482	2.817
^{27}Al	^{24}Na	1254	882.5	584.1	343.4	254.1	131.2	61.62	17.40	4.488	2.453
^{59}Co	^{58}Co	5321	3875	2577	1596	1233	665.5	320.2	158.9	21.72	14.33
^{59}Co	^{59}Fe	539.3	388.3	257.4	152.9	125.2	68.02	29.75	10.95	3.181	1.546

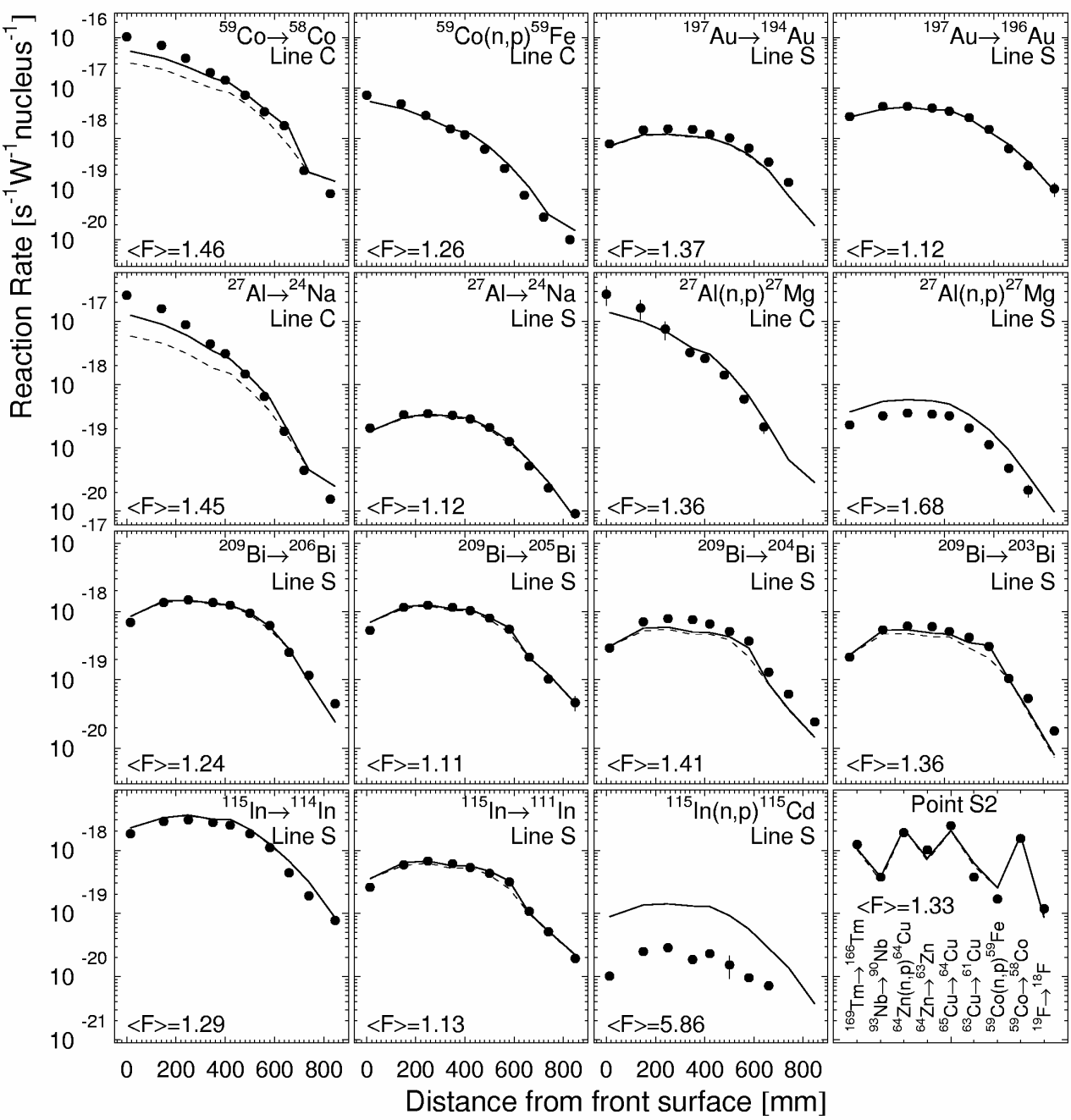

Fig. 7. The simulated and measured reaction rates. The dashed lines show the contribution from neutrons. Also shown is the mean squared factor of the simulation-experiment deviations.

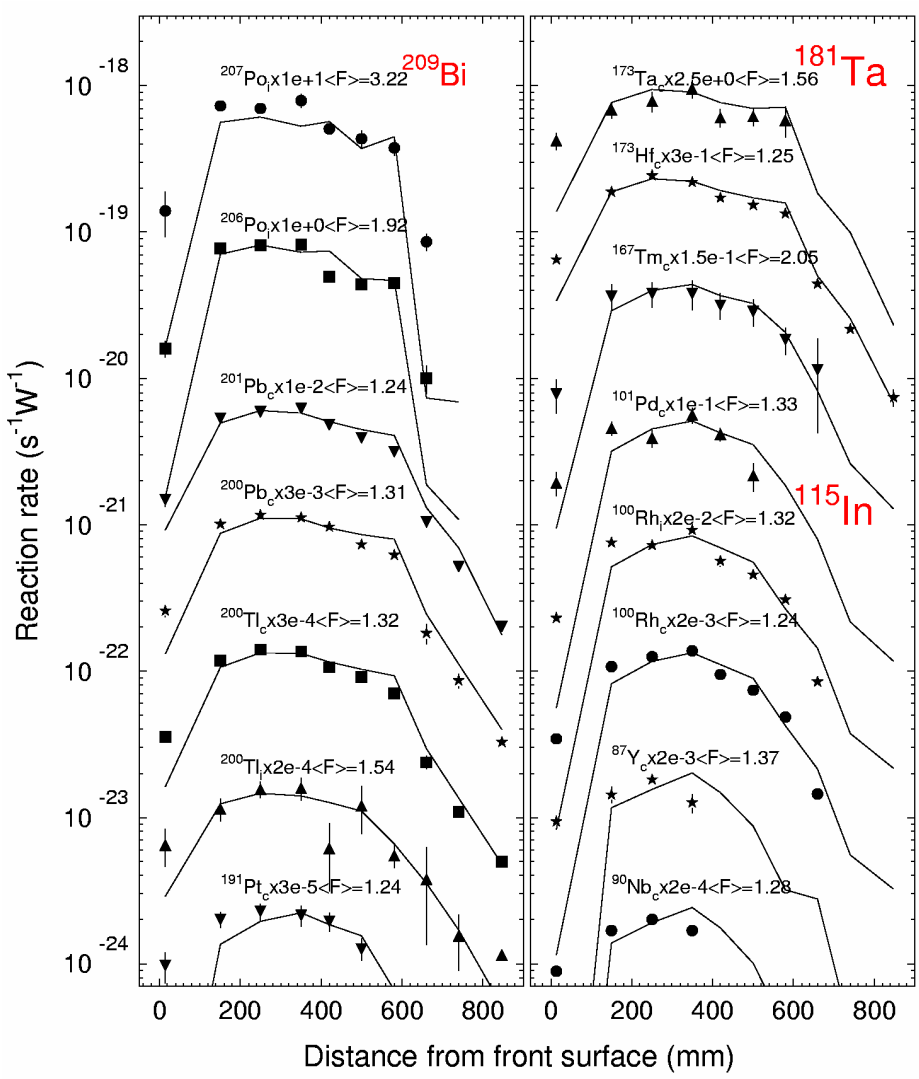

Fig. 8. The calculated and experimental RRs on ^{209}Bi, ^{181}Ta, and ^{115}In. The mean squared deviation factor <F> is presented for each reaction

Table 25. The simulated reaction rates at point S2 of W-Na target, $\left[10^{-20}\,\frac{1}{s\cdot nucleus\cdot W}\right]$.

Nucleus	Product	Reaction rate
^{169}Tm	^{166}Tm	104.6
^{93}Nb	^{90}Nb	37.40
^{64}Zn	^{64}Cu	217.6
^{64}Zn	^{63}Zn	74.13
^{65}Cu	^{64}Cu	202.6
^{63}Cu	^{61}Cu	61.84
^{59}Co	^{59}Fe	25.54
^{59}Co	^{58}Co	171.9
^{19}F	^{18}F	8.590

4. Calculation-to-experiment comparisons

From Fig. 7 it follows that most of the reaction rates are predicted up to a satisfactory accuracy (almost 50% of the calculated values are less than 30% different from the experimental data. At the same time, Fig. 7 shows also some systematical deviations of simulation from experiment, namely,

◊ the calculation results are significantly (up to a factor 2) underestimated at the first three points of line C;

◊ the calculation results are somewhat (up to factor 1.5) overestimated at the last point of line C;

◊ many of the results tend to being overestimated at the first point of line S;

◊ the $^{115}In(n,p)^{115}Cd$ reaction rate is very much (factor of above 5) overestimated.

The above-mentioned systematic differences are supposed to be accounted for as follows.

1. From Fig. 7 it follows that the proton contribution to the rates of the $^{59}Co \rightarrow ^{58}Co$ and $^{27}Al \rightarrow ^{24}Na$ reactions is significant at the first points of line C. The line C is located right on the proton beam axis, so the beam geometry parameters affect much the proton fluxes at those points. Therefore, the actual substantial deviations of the simulated reaction rates from the experiment at the first points of line C, together with the insignificant deviations at the next-in-turn points of line C, as well as at the points of line S, suggest all that the Gaussian beam shape should be regarded as but an insufficient approximation;
2. At the last point of line C, the major contribution to the $^{59}Co \rightarrow ^{58}Co$ and $^{27}Al \rightarrow ^{24}Na$ reaction rates is from the high-energy (above 20 MeV) neutrons. The contributions from slow neutrons and secondary protons are understated because that point was at the greatest distance from the target front surface. The LAHET code is inadequate in the case of generation and subsequent transport of the pre-equilibrium energy neutrons, and this can well explain the experiment-simulation difference at that particular point;
3. At the first point of line S, the major contribution to the reaction rates is from neutrons and secondary protons produced in hadron-nucleus interactions accompanied by the “side” and backward ejection. A small underestimation of the reaction rates observed for some reactions at that particular point suggests that the LAHET code simulates the backward neutron ejection but insufficiently;
4. The experiment has determined the ^{115g}Cd ($T_{1/2}$=53.46 h) production rate, while the simulation has given ^{115}Cd to be a sum of all states (ground + isomeric). Therefore, the observed difference does not indicate any inadequacy of the simulation.

Conclusion

The following important remark is apt here. Our experimental values of the reaction rates were mainly determined in terms of cumulative yields of the respective reaction products, whereas the simulated values were calculated from the independent yields. Strictly speaking, this approach is not quite correct, but the cumulative and independent yields measured for some nuclides (^{206}Bi and ^{57}Co, for instance) are coincident within the experimental errors, so our approach is justified to an extent. Nevertheless, the necessity for a rigorous analysis of the production conditions for the precursors of the measured nuclides has been quite obvious, and the analysis will be made in the further researches.

From Table 23 it follows that 24 reaction rates were scheduled to measure in the Project Workplan. This means that we had to measure 112 the reaction rates. Actually, 158 reaction rates have been measured, with the reaction rates measured totaling to 1070. At present, 22 reaction rates have been simulated. Two reactions, namely, $^{12}C(n,2n)^{11}C$ and $^{115}In(n,n')^{115}In$

have not been simulated, for their cross sections are absent from the ENDF/B-V library. The remaining reactions are being simulated. Most of the remaining reactions are difficult to simulate because of the limited energy range presented in the now accessible MENDL2 and MENDL2P libraries for the neutron and proton cross sections. The cross sections in the remaining energy range (above 100 MeV) must be supplemented with their simulation by the present-day codes that simulate the high-energy hadron-nucleus interactions.

References

[1] ISTC 839B-99, Final Project Technical Report of ISTC 839B-99, "Experimental and Theoretical Study of the Yields of Residual Product Nuclei Produced in Thin Targets Irradiated by 100-2600 MeV Protons", February 2001.

[2] J. Tobailem, "Sections Efficaces des Reactions Nucleaires Indutes par Protons, Deutrons, Particles Alphas. V. Silicium", Note CEA-N-1466(5), Saclay, 1981.

[3] Yu.E. Titarenko, O.V. Shvedov, V.F. Batyaev, et al., Cross sections for nuclide production in 1 GeV proton-irradiated ^{208}Pb, LANL Report LA-UR-00-4779 (2000); submitted to Phys. Rev C. (2001).

[4] R.E. Prael, H.Lichtenstein, LANL Report LA-UR-89-3014 (1989).

[5] Yu.N. Shubin et al., Cross Section Data Library MENDL-2 to Study Activation and Transmutation of Materials Irradiated by Nucleons of Intermediate Energies, IAEA, INDC(CCP)-385, Vienna, May 1995.

[6] Yu.N. Shubin et al., Cross Section Data Library MENDL-2p to Study Activation and Transmutation of Materials Irradiated by Nucleons of Intermediate Energies, Nuclear Data for Science and Technology (Trieste 1997), IPS, Bologna, 1997, v.1., p.1054.

Nuclear Data Section
International Atomic Energy Agency
Vienna International Centre, P.O. Box 100
A-1400 Vienna
Austria

e-mail: services@iaeand.iaea.org
fax: (43-1) 26007
telephone: (43-1) 2600-21710
Web: http://www-nds.iaea.org